Ultrafast Science
A SCIENCE PARTNER JOURNAL

RESEARCH ARTICLE

High-performance γ-MnO_2 Dual-Core, Pair-Hole Fiber for Ultrafast Photonics

Xiaohui Li[1*†], Xiangzhen Huang[1†], Yueheng Han[1], Enci Chen[2], Penglai Guo[3], Wenmin Zhang[1], Mingqi An[1], Zhiwen Pan[1], Qian Xu[1], Xiaoxiao Guo[1], Xiwei Huang[1], Yishan Wang[4], and Wei Zhao[4]

[1]School of Physics and Information Technology, Shaanxi Normal University, Xi'an 710000, Shaanxi, China. [2]School of Electronic Engineering, Guangxi University of Science and Technology, Liuzhou 545006, Guangxi, China. [3]School of Computer Science and Engineering, Macau University of Science and Technology, Taipa 999078, Macau, China. [4]State Key Laboratory of Transient Optics and Photonics, Xi'an Institute of Optics and Precision Mechanics, Chinese Academy of Sciences, Xi'an 710119, Shaanxi, China.

*Address correspondence to: lixiaohui0523@163.com
†The authors contributed equally to this work

Citation: Li X, Huang X, Han Y, Chen E, Guo P, Zhang W, An M, Pan Z, Xu Q, Guo X, et al. High-performance γ-MnO_2 Dual-Core, Pair-Hole Fiber for Ultrafast Photonics. *Ultrafast Sci.* 2023;3:Article 0006. https://doi.org/10.34133/ultrafastscience.0006

Submitted 26 October 2022
Accepted 30 November 2022
Published 16 January 2023

Manganese dioxide (MnO_2) is a widely used and well-studied 3-dimensional (3D) transition metal oxide, which has advantages in ultrafast optics due to large specific surface area, narrow bandgap, multiple pores, superior electron transfer capability, and a wide range of light absorption. However, few studies have considered its excellent performance in ultrafast photonics. γ-MnO_2 photonics devices were fabricated based on a special dual-core, pair-hole fiber (DCPHF) carrier and applied in ultrafast optics fields for the first time. The results show that the soliton molecule with tunable temporal separation (1.84 to 2.7 ps) and 600-MHz harmonic solitons are achieved in the experiment. The result proves that this kind of photonics device has good applications in ultrafast lasers, high-performance sensors, fiber optical communications, etc., which can help expand the prospect of combining 3D materials with novel fiber for ultrafast optics device technology.

Introduction

Three-dimensional (3D) transition metal oxides have traditionally functional material of interest, mostly with narrow energy bandwidths and often as insulators with antiferromagnetic configurations [1,2]. Therefore, 3D transition metal oxides have a series of very peculiar physical phenomena that exhibit properties significantly different from those of conventional metals and semiconductors. In addition, because of the diversity of valence states of transition metals, it is possible to synthesize a variety of oxides with different combinations of different morphologies, so that they have their unique optical, electrical, and magnetic properties, which make them important for applications and research in photodetection [3–5], saturable absorption [6,7], catalysts [8,9], and sensors [10–12]. The more widely studied and applied ones are Mn_xO_y, Fe_xO_y, Co_xO_y, Ni_xO_y, etc. In 2017, Mao et al. [13] achieved Q-switched pulse output using Fe_3O_4 as a saturable absorber (SA); in 2020, Rizman et al. [14] achieved Q-switched pulse output based on NiO as a SA; in 2021, Li et al. [15] achieved mode-locked pulsed output based on Co_3O_4 as a saturable absorber. Although many results have been obtained in the study of transition metal oxides for ultrafast optics, the research still needs to be further expanded compared to numerous transition metal oxides. For example, manganese dioxide (MnO_2), the most widely used of Mn_xO_y, has been little studied for ultrafast optics applications; in 2016, Hattori et al.[16] achieved Q-switched output using MnO_2 in an Yb-doped fiber laser, and in 2020, Heng et al. [17] completed Q-switched operation using MnO_2 nanosheets in an Er-doped fiber laser. MnO_2 can form many different configurations (α-MnO_2, β-MnO_2, γ-MnO_2, and δ-MnO_2) by different common prongs or shared vertices due to its crystal structure unit of [MnO_6] octahedra [18]. Among them, γ-MnO_2 is a microsphere formed by the self-assembly of nanosheets, which has the structural characteristics of a narrow bandgap and high specific surface area common to MnO_2, and the irregularity of cell growth makes defects and vacancies arise, which makes the structure have many advantages of multipore and large contact area, good interaction with light, and stable performance structure in air environment [19–22], so it is suitable for making novel photonics devices.

Most of the current methods of making photonics devices by combining materials with novel fibers have the problems of short interaction length between light and materials and difficulty in preservation, which is therefore difficult to mass produce and preserve for a long time. Thus, it is a new exploration direction to find a carrier that is stable and can interact with the material at a relatively long distance to make photonics devices. The fiber with a hollow structure is highly popular in the fabrication of many photonic devices because of its good

sealing, special microstructure, and excellent performance in supporting high power [23–26]. In some works, photonics devices have been fabricated using fibers with hollow structures as carriers with good results. In 2015, Gao et al. [27] obtained dissipative soliton output using photonic crystal fiber (PCF) filled with Bi_2Se_3 as SA; in 2016, Li et al. [28] obtained mode-locked pulse output using PCF filled with carbon nanotubes as SA; and in 2020, Zuo et al. [29] obtained stretched-pulse output using PCF filled with MoS_2 as SA. Until now, researchers are still exploring the options of combining special fiber with novel materials to achieve the effect that is similar with artificial SAs [30]. However, the hollow aperture of conventional PCF fiber is too small for material filling, while the special fiber with a large hollow aperture has the structural feature of easy filling, which is equivalent to a microvessel and can control the action distance. Compared with D-shaped, tapered fiber, and sandwich type, the dual-core, pair-hole fiber (DCPHF) is a good platform due to without processing and excellent sealing performance [31,32]. Adding the new material as a modulation medium also allows adding some external control methods to achieve more parameter modulation.

In this paper, we utilized a DCPHF as a carrier to fill γ-MnO_2 into the fiber using capillary action to fabricate a novel photonics device. We applied this device to the Er-doped fiber laser to achieve the pulse output of 1,561 nm, and the pulse width is 967.5 fs. We also achieved soliton molecules output with center wavelengths at 1,560.6 and 1,561.4 nm. The corresponding modulation period is 3 and 4.4 nm, respectively. In addition, we achieved 37th (600 MHz) harmonic soliton with a pulse width of 1.18 ps in 1,561 nm. The results show that this γ-MnO_2 DCPHF has excellent performance and application prospects in nonlinear fiber optics and ultrafast photonics [33–38].

Materials and Methods

The γ-MnO_2 synthesized by hydrothermal method [39]: First, 4.575 g of $(NH_4)_2S_2O_8$ and 3.375 g of $MnSO_4{\cdot}H_2O$ were weighed; then the 2 drugs were dissolved in 400 ml of deionized water; and after they were fully dissolved, the drugs were transferred to a polytetrafluoroethylene-sealed autoclave. The hydrothermal reaction was continued for 24 hours at 90 °C under atmospheric pressure. Then, the precipitate of the above drug was filtered and washed with deionized water until the pH value reached about 7. Last, the product was calcined at 300 °C for 4 hours to synthesize γ-MnO_2 microspheres.

To characterize the properties of γ-MnO_2, we have performed material characterization of the prepared γ-MnO_2. Figure 1A provides the scanning electron microscope (SEM) images of the γ-MnO_2 material in the scale range of 2 μm. γ-MnO_2 presents a sea urchin-like structure with a diameter of about 6 μm in the image self-assembled from strips of nanosheets. The elemental mapping of γ-MnO_2 is shown in Fig. 1B and C. In Fig. 1D to F, TEM images were measured at 2-μm, 500-nm, and 5-nm magnification sizes, respectively. The image analysis reveals that the sample consists of striped nanosheets composed of sea urchin-like microspheres, and a (120) crystal plane with a lattice spacing of 0.396 nm can be detected in its long striped nanosheets, corresponding to the γ-MnO_2 sample in orthorhombic phase.

To analyze more accurately the elemental composition, chemical state, and molecular structure of MnO_2, the x-ray photoelectron spectroscopy (XPS) was characterized. Figure 1G shows the full spectrum of the sample, demonstrating the presence of Mn 2s, Mn 2p, O 1s, and C 1s. The XPS spectrum of Mn at 653.3 and 641.8 eV in Fig. 1H are attributed to the self-selected orbital splitting of Mn $2p_{1/2}$ and Mn $2p_{3/2}$. The binding energy peaks of O 1s in Fig. 1I are 529.3 and 531.6 eV from lattice oxygen and surface-adsorbed oxygen, respectively. To know the crystal structure of MnO_2 more accurately, we characterized the sample by x-ray diffraction (XRD), as shown in Fig. 1J, and the obtained results have abundant spectral lines of (120), (031), (131), (300), and (160), which are agreed with the standard card (PDF#14-0644). XRD pattern diffraction peaks are weak, which is related to the ultrathin structure and the presence of surface amorphous states, as shown by the SEM and transmission electron microscopy (TEM) results. In addition, Raman spectra were also measured, and Fig. 1K shows the characteristic peak at 645 cm^{-1} corresponding to the Mn–O lattice vibration. Figure 1L also shows the cell structure of γ-MnO_2.

Figure 2A shows the basic transverse structure of the DCPHF, in which there are 2 cores, both 10.7 μm in diameter, and 2 air holes of 38.9 μm in diameter. The DCPHF is a commercial product from Yangtze Optical Electronic Co. Ltd. This structure allows the core to be fused to a single-mode fiber with low loss and the 2 air holes to be filled with materials. First, the dispersion with a 1:1 volume ratio of γ-MnO_2 nanoparticles and anhydrous ethanol was prepared. The γ-MnO_2 nanoparticles were gradually added to the anhydrous ethanol and shaken well until the dispersion showed a relatively colorful dark brown. Then, the dispersion was ultrasonicated for 1 h to make the agglomerated nanomaterials disperse into one small nanoparticle. The fiber was then stripped of the coating layer at both ends of the fiber using a pair of wire strippers, and the ends of the fiber were wiped clean with anhydrous ethanol paper. Figure 2C shows the schematic of the γ-MnO_2 DCPHF structure.

The fiber filled with the dispersion was then placed under a microscope to observe that a large amount of dispersion had entered the air holes of the fiber and that the particles of the dispersion were dispersed equally without larger clusters of large particles. Immediately afterward, the fiber was placed in a drying oven for 20 min, and the temperature was set to 55 °C. Because of the uniform heating, the γ-MnO_2 nanoparticles will be deposited on the wall of the air hole. The dried fiber continues to be placed under the microscope, and it is found that the anhydrous ethanol has completely evaporated and the γ-MnO_2 nanoparticles are uniformly adsorbed on the tube walls of the air holes of the fiber without relatively large agglomerated particles.

It should be noticed that the temperature should not be set too high when drying the filled fiber because heating too fast will cause the anhydrous ethanol to evaporate and will affect the uniform distribution of the material in the air holes. To make this filling production method with better repeatability, we summarized the above production process in the production process. Figure 2B shows the distribution of the material in the DCPHF and the air hole under the optical microscope. Subsequently, the material-filled fiber was removed, and the residual material was wiped off again with mirror paper and fused to the single-mode fiber. Thus, the preparation of γ-MnO_2 DCPHF is completed. When we tested its nonlinear absorption properties, we found that different filling lengths and filling concentrations affect its nonlinear absorption results and that this nonlinear absorption is regular, can be controlled

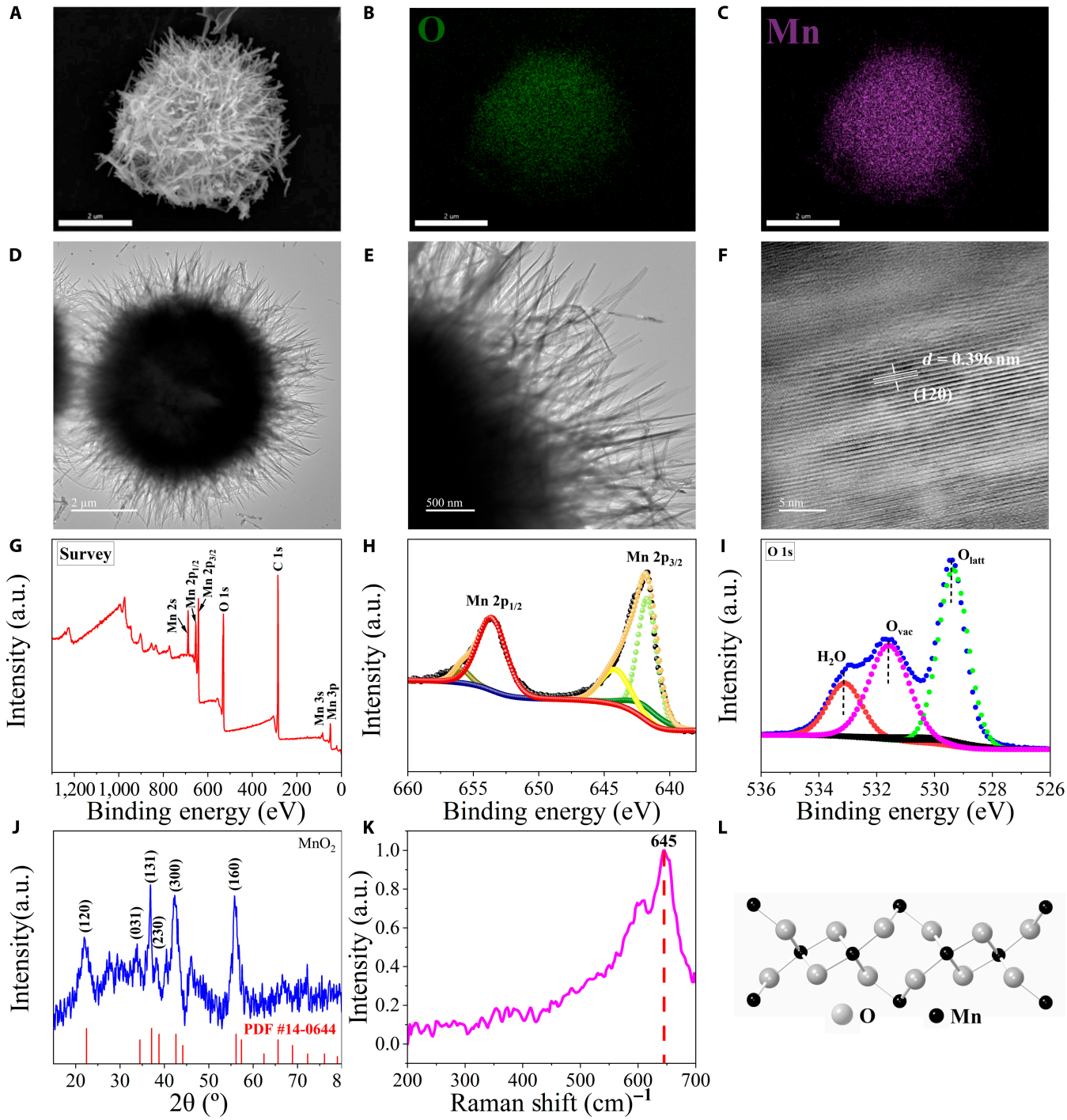

Fig. 1. (A) Scanning electron microscope (SEM) image of γ-MnO_2. (B and C) The energy-dispersive x-ray spectroscopy elemental mappings of γ-MnO_2. (D to F) High-resolution TEM images of γ-MnO_2 at 2 μm, 500 nm, and 5 nm. (G to I) XPS of γ-MnO_2. (J) Surface XRD pattern of γ-MnO_2. (K) Raman spectrum. (L) The lattice structure of γ-MnO_2. a.u., arbitrary units.

artificially, and can be repeatedly operated. Too longer fill lengths and large fill concentrations lead to excessive linear absorption losses, which are not favorable for the γ-MnO_2 DCPHF's application as an SA but benefit the generation of nonlinear harmonic. γ-MnO_2 DCPHF with different filling lengths and different fill concentrations are suitable for different nonlinear optical applications. The nonlinear optical properties of the γ-MnO_2 DCPHF SA were measured using the same double-equilibrium detection system. The nonlinear transmission result can be found in Fig. S1.

Results and Discussion

A 10-cm-long γ-MnO_2 DCPHF as an SA is fused to single-mode fiber (SMF) and then inserted in a fiber laser as shown in Fig. 3A. A 60-cm-long Lekki EDF110-4/125 is the gain media. The gain

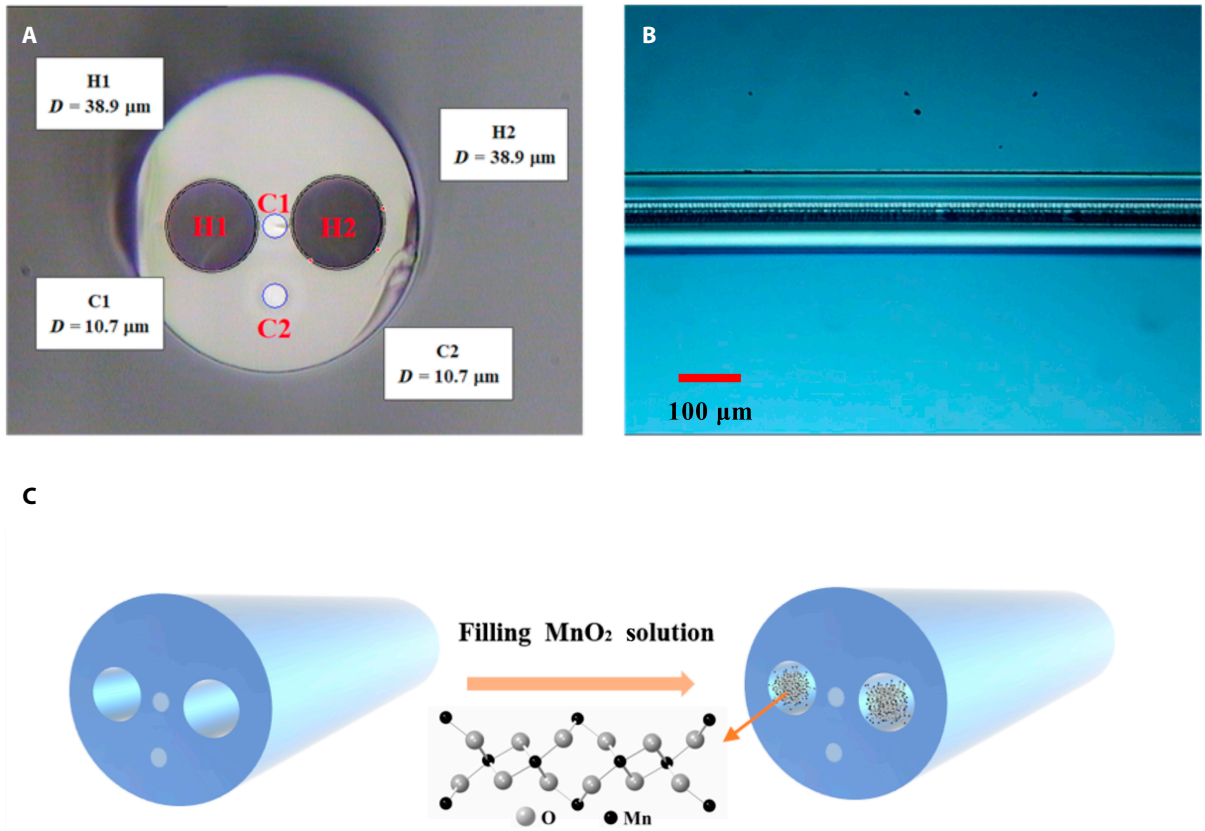

Fig. 2. DCPHF and saturable absorber filled with γ-MnO_2 nanomaterial. (A) Dual-core, pair-hole fiber. (B) Air hole filled with γ-MnO_2 nanomaterial. (C) Filling process schematic.

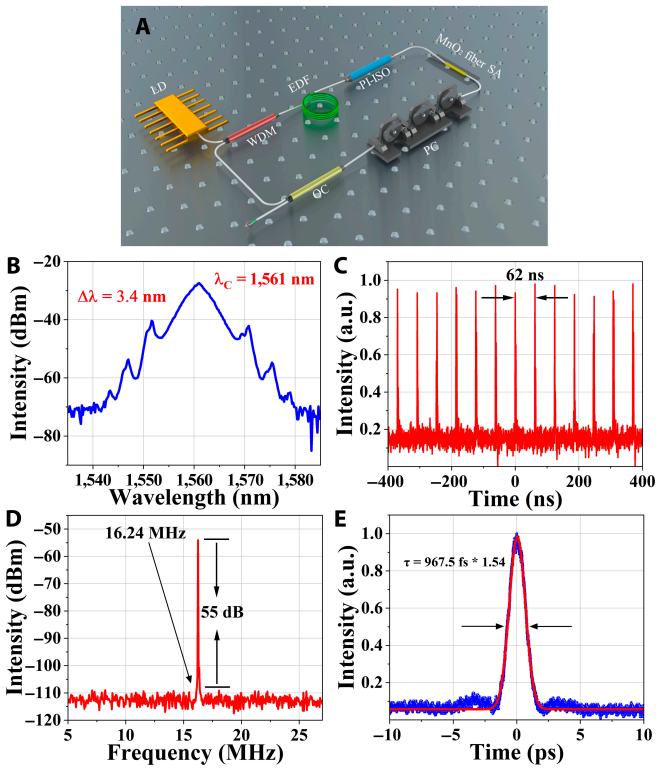

Fig. 3. (A) Experimental schematic of mode-locked laser with γ-MnO_2 DCPHF. The spectrum (B), pulse train (C), RF spectrum (D), and autocorrelation trace (E) at pump power of 57.4 mW.

media is pumped by a 976-nm laser diode (LD). In this case, the LD serves as the pump source for the fiber laser, and the wavelength-division multiplexer (WDM) serves to couple the pumped light in the resonant cavity, polarization independent isolator (PI-ISO) controlling the transmission of the laser direction. The laser cavity length is 12.6 m. All fibers are SMF from Corning, except for a 0.6-m long erbium-doped fiber (EDF) and a small section of the DCPHF.

Before using γ-MnO_2 DCPHF, we first studied the situation of the output pulses when DCPHF without filling MnO_2 was placed into the cavity. No matter how the pump power and polarization controller (PC) were adjusted, only continuous waves could be shown in the spectrum. The polarization-dependent loss was measured at 0.4 dB. Thus, the possibility of mode locking caused by the nonlinear polarization rotation (NPR) was excluded.

We used an oscilloscope and an autocorrelator to measure the obtained laser in the time domain, as well as a spectrometer to make measurements in the frequency domain. Among them, the digital oscilloscope (Rigol DS6104) at 1 GHz was combined with a photodetector (Thorlabs DET01CFC) at 2-GHz bandwidth to record the pulse sequence of the laser, and the autocorrelator (FR-103XL) was used to record the pulse width, and the spectrum analyzer (Anritsu MS9710C) recorded the central wavelength and spectral width of the laser. A spectrum analyzer (Rohde & Schwarz FSC6) with a bandwidth of 6 GHz and a photodetector were combined to measure the repetition frequency of the laser. The γ-MnO_2 DCPHF is placed in the cavity as a photonics device to achieve the output of mode-locked pulses. A 3:7 fiber optical coupler (OC) couples 30% of the laser output for use in oscilloscopes and spectrum analyzers to detect laser characteristics.

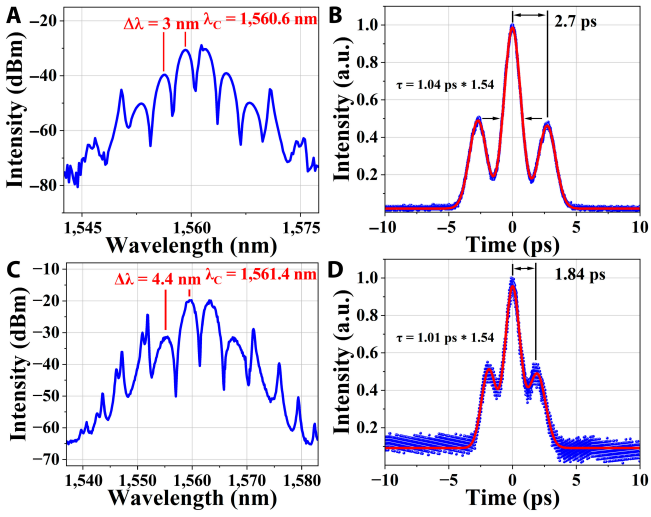

Fig. 4. The spectrum (A) and the autocorrelation trace (B) in 78.5 mW of pump power. The spectrum (C) and the autocorrelation trace (D) in 164 mW of pump power.

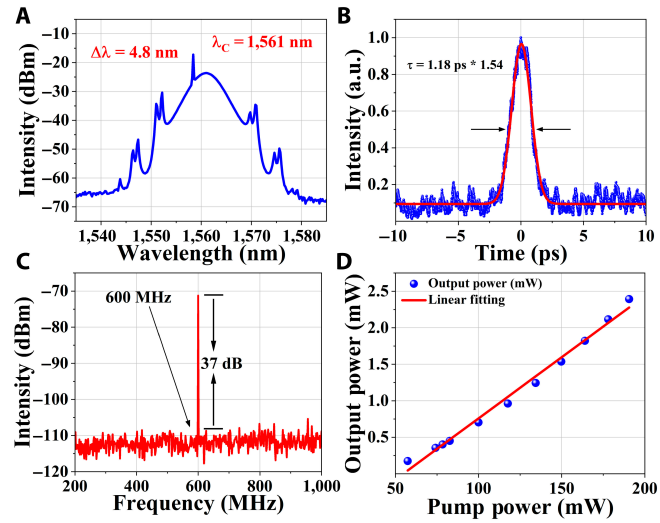

Fig. 5. The spectrum (A), autocorrelation trace (B), and RF spectrum (C) of 178 mW of pump power. (D) Output power versus pump power.

On the basis of the above structure, the pump power was increased, and we achieved the fundamental soliton in 74.16 mW of pump power. When the pump power was reduced to 57.4 mW, the pulse state as shown in Fig. 3. Figure 3B shows a spectrum with 0.05-nm resolution, the center wavelength is 1,561 nm, and the spectrum width is 3.4 nm. The real-time pulse sequence is recorded in Fig. 3C, and the pulse interval is accurately measured as 62 ns. Figure 3D shows the radio frequency (RF) spectrum that the repetition rate is 16.24 MHz, in which the resolution bandwidth (RBW) is 1 kHz. The autocorrelation trace is shown in Fig. 3E, and the $sech^2$ fitting is 967.5 fs.

With the pump power adjusted to 78.5 mW, we successfully achieved soliton molecules. Subsequently, we adjusted the pump power to 164 mW to get another soliton molecule to state recorded the results as shown in Fig. 4. The soliton molecules spectrum at 78.5 mW was recorded in Fig. 4A. In this spectrum, the center wavelength is 1,560.6 nm and the modulation period is 3 nm. Figure 4B is the autocorrelation trace corresponding to Fig. 4A that the pulse width is 1.04 ps by hyperbolic secant function fitting and the pulse interval is 2.7 ps. When the pump power increases to 164 mW, another soliton molecules' spectrum and autocorrelation trace were recorded as in Fig. 4C and D, respectively. The spectrum in Fig. 4C demonstrates that the center wavelength is 1,561.4 nm and the modulation period is 4.4 nm. The corresponding autocorrelation trace in Fig. 4D shows that the pulse width is 1.01 ps and the pulse interval is 1.84 ps.

We realized that the high-order harmonic (37th) soliton with a repetition rate of 600 MHz is in 178 mW of pump power. Figure 5A to C shows the spectrum, autocorrelation trace, and RF spectrum, respectively. The 37th-order harmonic soliton's center wavelength is 1,561 nm and the spectrum width is 4.8 nm. In addition, the repetition rate is 600 MHz with the signal-noise ratio (SNR) being 37 dB in Fig. 5C, in which the RBW is 1 kHz. We also measured the autocorrelation curve and fitted it with $sech^2$ shown in Fig. 5B, which the pulse width is 1.18 ps. The 600-MHz harmonic soliton is also the result of the highest repetition frequency achieved by similar schemes to the best that we know. Because of its structural peculiarities, the DHPHF has a higher nonlinear coefficient than the SMF. Moreover, the γ-MnO_2 DCPHF with low saturation absorption intensity will lead to easier pulse splitting to achieve stable high-order harmonic soliton. Our scheme validates the possibility of achieving high-order harmonic soliton. The pulse trains about harmonic soliton were shown in Fig. S3. Figure 5D shows the correlation between output power and pump power with a slope efficiency of 1.675%, which is similar to the slope efficiency of most ring cavity structures such as NPR structure.

Conclusion

In conclusion, we successfully synthesized γ-MnO_2 DCPHF with controllable fiber length and filling concentration. Thus, the nonlinear application, such as the all-fiber mode-locked laser, has been realized with a combination between strong light–matter interaction and less loss. The controlling massive manufacturing filling method and excellent nonlinear optical phenomenon demonstrate its superiorities compared with similar photonics devices. In addition, γ-MnO_2 DCPHF can be further extended in various optical applications, such as optical frequency comb, and nonlinear harmonic generation.

Acknowledgments

Funding: This research was supported by the Starting Grants of Shaanxi Normal University (grant nos. 1112010209 and 1110010717), Fundamental Research Funds for the Central Universities (no. GK202103013 and 2021CSLY005), and funded projects for the Academic Leader and Academic Backbones, Shaanxi Normal University (no. 18QNGG006)

Supplementary Materials

Figs. S1 to S3

References

1. Imada M, Fujimori A, Tokura Y. Metal-insulator transitions. *Rev Mod Phys*. 1998;70(4):1039–1263.

2. Patterson JR, Aracne CM, Jackson DD, Malba V, Weir ST, Baker PA, Vohra YK. Pressure-induced metallization of the Mott insulator MnO. *Phys Rev B*. 2004;69(22):220101.
3. Xu L, Xia J, Wang L, Qian J, Li H, Wang K, Sun K, He M. α-Fe_2O_3 cubes with high visible-light-activated photoelectrochemical activity towards glucose: Hydrothermal synthesis assisted by a hydrophobic ionic liquid. *Chemistry*. 2014;20(8):2244–2253.
4. Sun L, Wang C, Ji T, Wang J, Yi G-C, Chen X. Self-powered UV-visible photodetector with fast response and high photosensitivity employing an Fe:TiO_2/n-Si heterojunction. *RSC Adv*. 2017;7(81):51744–51749.
5. Guan M, Chen D, Hu S, Zhao H, You P, Meng S. Theoretical insights into ultrafast dynamics in quantum materials. *Ultrafast Sci*. 2022;2022:9767251.
6. Zhao Y, Wang W, Li X, Lu H, Shi Z, Wang Y, Zhang C, Hu J, Shan G. Functional porous MOF-derived CuO octahedra for harmonic soliton molecule pulses generation. *ACS Photonics*. 2020;7(9):2440–2447.
7. Liu M, Liu W, Liu X, Ouyang Y, Hou H, Lei M, Wei Z. Yttrium oxide as a Q-switcher for the near-infrared erbium-doped fiber laser. *Nano*. 2020;9(9):2887–2894.
8. Yu X, He J, Wang D, Hu Y, Tian H, He Z. Facile controlled synthesis of Pt/MnO_2 nanostructured catalysts and their catalytic performance for oxidative decomposition of formaldehyde. *J Phys Chem C*. 2011;116(1):851–860.
9. Fan Z, Zhang Z, Fang W, Yao X, Zou G, Shangguan W. Low-temperature catalytic oxidation of formaldehyde over Co_3O_4 catalysts prepared using various precipitants. *Chin J Catal*. 2016;37(6):947–954.
10. Ren X, Chen D, Meng X, Tang F, Hou X, Han D, Zhang L. Zinc oxide nanoparticles/glucose oxidase photoelectrochemical system for the fabrication of biosensor. *J Colloid Interface Sci*. 2009;334(2):183–187.
11. Zhang X, Zhao Y, Li S, Zhang S. Photoelectrochemical biosensor for detection of adenosine triphosphate in the extracts of cancer cells. *Chem Commun*. 2010;46(48):9173–9175.
12. Sun B, Zhang K, Chen L, Guo L, Ai S. A novel photoelectrochemical sensor based on PPIX-functionalized WO_3-rGO nanohybrid-decorated ITO electrode for detecting cysteine. *Biosens Bioelectron*. 2013;44:48–51.
13. Mao D, Cui X, Zhang W, Li M, Feng T, Du B, Lu H, Zhao J. Q-switched fiber laser based on saturable absorption of ferroferric-oxide nanoparticles. *Photonics Res*. 2017;5(1):52–56.
14. Rizman ZI, Zulkipli NF, Arof H, Yasin M, Harun SW. Q-switched and tunable wavelength fiber laser utilizing nickel oxide saturable absorber and sagnac loop mirror filter. *Infrared Phys Technol*. 2020;109:103433.
15. Li X, An M, Li G, Han Y, Guo P, Chen E, Hu J, Song Z, Lu H, Lu J. MOF-derived porous dodecahedron rGO-Co_3O_4 for robust pulse generation. *Adv Mater Interfaces*. 2022;9(5):2101933.
16. Hattori HT, Khaleque A, Liu L, Greck MR. Ytterbium-doped Q-switched fiber laser based upon manganese dioxide (MnO_2) saturable absorber. *Appl Opt*. 2016;55(32):9226–9231.
17. Jia H, Li N, Li S, Liu J, Dong Y, Jia Z, Di W, Qin G, Qin W. MnO_2 nanosheets as saturable absorbers for a Q-switched fiber laser. *Opt Mater Exp*. 2020;10(12):3097–3106.
18. Brock SL, Duan N, Tian ZR, Giraldo O, Zhou H, Suib SL. A review of porous manganese oxide materials. *Chem Mater*. 1998;10(10):2619–2628.
19. Huo G, Wang X, Zhang Z, Song Z, Kang X, Chen M, Wang Q, Fu X, Luo J. γ-MnO_2 nanorod-assembled hierarchical microspheres with oxygen vacancies to enhance electrocatalytic performance toward the oxygen reduction reaction for aluminum-air batteries. *J Energy Chem*. 2020;51:81–89.
20. Hu J, Duan Y, Zhang J, Jing H, Liu S, Li W. γ-MnO_2/polyaniline composites: Preparation, characterization, and applications in microwave absorption. *Phys B Condens Matter*. 2011;406(10):1950–1955.
21. Julien C, Massot M, Rangan S, Lemal M, Guyomard D. Study of structural defects in γ-MnO_2 by Raman spectroscopy. *J Raman Spectrosc*. 2002;33(4):223–228.
22. Zhou M, Zhang X, Wang L, Wei J, Wang L, Zhu K, Feng B. Growth process and microwave absorption properties of nanostructured γ-MnO_2 urchins. *Mater Chem Phys*. 2011;130(3):1191–1194.
23. Knight JC, Birks TA, Cregan RF, Russell PSJ, de Sandro J-P. Large mode area photonic crystal fibre. *Electron Lett*. 1998;34:1347–1348.
24. Limpert J, Schmidt O, Rothhardt J, Röser F, Schreiber T, Tünnermann A, Ermeneux S, Yvernault P, Salin F. Extended single-mode photonic crystal fiber lasers. *Opt Express*. 2006;14(7):2715–2720.
25. Chen H, Li S, Ma M, Liu Y, Shi M, Liu Q, Cheng T. Filtering characteristics and applications of photonic crystal fibers being selectively infiltrated with one aluminum rod. *J Lightwave Technol*. 2016;34(21):4972–4980.
26. Ferreira MS, Bierlich J, Kobelke J, Schuster K, Santos JL, Frazão O. Towards the control of highly sensitive Fabry-Pérot strain sensor based on hollow-core ring photonic crystal fiber. *Opt Express*. 2012;20(20):21946–21952.
27. Gao L, Zhu T, Huang W, Luo Z. Stable, ultrafast pulse mode-locked by topological insulator Bi_2Se_3 Nanosheets interacting with photonic crystal fiber: From anomalous dispersion to Normal dispersion. *IEEE Photonics J*. 2015;7(1):1–8.
28. Li Y, Gao L, Huang W, Gao C, Liu M, Zhu T. All-fiber mode-locked laser via short single-wall carbon nanotubes interacting with evanescent wave in photonic crystal fiber. *Opt Express*. 2016;24(20):23450–23458.
29. Zuo Y, Yu W, Liu C, Cheng X, Qiao R, Liang J, Zhou X, Wang J, Wu M, Zhao Y, et al. Optical fibres with embedded two-dimensional materials for ultrahigh nonlinearity. *Nat Nanotechnol*. 2020;15(12):987–991.
30. Kobtsev SM. Artificial saturable absorbers for ultrafast fibre lasers. *Opt Fiber Technol*. 2022;68:102764.
31. Cheng P, Du Y, Han M, Shu X. Mode-locked and Q-switched mode-locked fiber laser based on a ferroferric-oxide nanoparticles saturable absorber. *Opt Express*. 2020;28(9):13177–13186.
32. Gladush Y, Mkrtchyan AA, Kopylova DS, Ivanenko A, Nyushkov B, Kobtsev S, Kokhanovskiy A, Khegai A, Melkumov M, Burdanova M, et al. Ionic liquid gated carbon nanotube saturable absorber for switchable pulse generation. *Nano Lett*. 2019;19(9):5836–5843.
33. Jin Q, E Y, Gao S, Zhang X. Preference of subpicosecond laser pulses for terahertz wave generation from liquids. *Adv Photonics*. 2020;2(1):015001.
34. Tegin U, Rahmani B, Kakkava E, Psaltis D, Moser C. Single-mode output by controlling the spatiotemporal nonlinearities in mode-locked femtosecond multimode fiber lasers. *Adv Photonics*. 2020;2(5):056005.
35. Yong J, Yang Q, Hou X, Chen F. Nature-inspired Superwettability achieved by femtosecond lasers. *Ultrafast Sci*. 2022;2022:9895418.

36. Song Y, Wang Z, Wang C, Panajotov K, Zhang H. Recent progress on optical rogue waves in fiber lasers: Status, challenges, and perspectives. *Adv Photonics*. 2020;2(2):024001.
37. Zhang Z, Zhang J, Chen Y, Xia T, Wang L, Han B, He F, Sheng Z, Zhang J. Bessel terahertz pulses from superluminal laser plasma filaments. *Ultrafast Sci*. 2022;2022:9870325.
38. Wang X, Liu X, Lu X, Chen J, Long Y, Li W, Chen H, Chen X, Bai P, Li Y, et al. 13.4 fs, 0.1 Hz OPCPA front end for the 100 PW-class laser facility. *Ultrafast Sci*. 2022;2022:9894358.
39. Zhang J, Li Y, Wang L, Zhang C, He H. Catalytic oxidation of formaldehyde over manganese oxides with different crystal structures. *Cat Sci Technol*. 2015;5(4):2305–2313.